Quantification of fracture interaction using stress intensity factor variation maps

Robin N. Thomas, Adriana Paluszny, and Robert W. Zimmerman

[1]Department of Earth Science and Engineering, Imperial College London, London, UK.

Key Points:

- Fractures are modelled using 3D finite element simulations
- Three measures are used to quantify the amount and type of interaction a fracture experiences
- Interaction maps demonstrate how interaction varies with fracture spacing and orientation

Corresponding author: Robin Thomas, `robin.thomas11@imperial.ac.uk`

Abstract

Accurate and flexible models of fracture interaction are sought after in the fields of mechanics and geology. Stress intensity factors (SIFs) quantify the energy concentrated at the fracture tips, and are perturbed from their isolated values when two fractures are close to one another. Using a three dimensional finite element fracture mechanics code to simulate static fractures in tension and compression, interaction effects are examined. SIF perturbations are characterised by introducing three interaction measures: the circumferential and maximum SIF perturbation provide the 'magnitude' of the effect of interaction, and the amplification to shielding ratio quantifies the balance between increased and decreased SIFs along the tip. These measures are used to demonstrate the change in interaction with fracture separation, and to find the separation at which interaction becomes negligible. Interaction maps are constructed by plotting the values of the interaction measures for a static fracture as a second fracture is moved around it. These maps are presented for several common fracture orientations in tension. They explore interaction by highlighting regions in which growth is more likely to occur and where fractures will grow into non-planar geometries. Interaction maps can be applied to fracture networks with multiple discontinuities to analyse the effect of geometric variations on fracture interaction.

1 Introduction

Fracture interaction in brittle rocks is of great interest at a variety of scales. Fractures alter the surrounding stress state of the medium, enhancing or reducing stress depending on the mode of deformation, location and fracture orientation [*Olson and Pollard*, 1991]. Predicting the behaviour of a fracture system requires a thorough understanding of the stress state within the material, and the current fracture geometries. This is not straightforward to characterise in many settings, particularly for geological materials due to their heterogeneity, anisotropy, and the uncertainty of subsurface characteristics relative to exposed outcrops. At smaller scales, linkage of fractures has a large control on the hydraulic properties of rocks and reservoirs, with implications for hydrocarbon production [*Nelson*, 2001] and radioactive waste disposal [*Tsang et al.*, 2015]. At larger scales, interactioln effects are a key control over the formation of geological structures [*Delaney and Pollard*, 1981], rift evolution [*Gawthorpe and Leeder*, 2000] and fault slip during earthquakes [*Zachariasen and Sieh*, 1995; *Green et al.*, 2015]. Determining when faults transition from soft to hard-linkage requires accurate observations and a detailed history of displacement [*Duffy et al.*, 2015].

When a fracture is present in a tensile stress field, it alters the stress in its local area, in two ways [*Price and Cosgrove*, 1990; *Rives et al.*, 1992; *Kachanov*, 1993]. First, a fracture generates a shielding zone around its surface, also known as a stress shadow, in which local stress is reduced. Second, at the tip of a fracture, an amplification zone is generated, also known as the concentration zone, in which local stress is increased. When another fracture enters these zones, this change in stress results in significant changes to its behaviour. When the fractures are similar in size, they induce a reciprocal effect upon one another. In full 3D space, this interaction is complex, and the change in stress varies significantly over each fracture, particularly when fractures are overlapped. Interaction is important because it may both enhance and preclude growth, and is a controlling mechanism of the self-organisation of fracture patterns. In turn, self-organisation may influence the ensuing mechanical and flow properties of the fracture pattern [*Olson and Pollard*, 1991; *Olson*, 2004].

Numerical simulations are instrumental in understanding fracture interaction. A variety of techniques have been utilised to numerically model fractured geological media [*Jing and Hudson*, 2002], many of which include discrete fractures. Three main approaches can be distinguished: stress-based, debonding-based, and SIF-based. Stress-based methods usually rely on displacement fields generated by the finite element method (FEM) [*Carter*

et al., 2000; *Riahi et al.*, 2010; *Rabczuk*, 2013; *Pouya*, 2015]. They rely on measurements of stresses local to the fracture tips, and therefore require significantly refined meshes. Debonding-based methods are routinely used in conjunction with the distinct or discrete element methods [*Lisjak and Grasselli*, 2014; *Lei et al.*, 2017], and model rock mass interaction as agglomerate rock matrices made up of bonded particles, which mimic the development of fractures by releasing element bonds when local stresses are exceeded. Debonding methods follow the pre-existing discretisation, and require the definition of micro-scale properties using calibration tests that are rock type and scale dependent.

Stress intensity factor (SIF) based fracture modelling has received great attention in material design to predict failure [*Stonesifer et al.*, 1993; *Moussa*, 2002; *Busfield et al.*, 2005; *Kamaya*, 2008a]. SIFs provide an effective method for analysing fracture propagation and interaction [*Paris and Erdogan*, 1963; *Lam and Phua*, 1991]. They are one of several methods of fracture analysis, quantifying the energy released at a fracture tip during crack growth [*Irwin*, 1956; *Anderson and Anderson*, 2005]. They can be used to evaluate failure criteria for modelling fracture propagation [*Paris and Erdogan*, 1963; *Brace*, 1960; *Lawn*, 1993]. They have become a key part of fitness-for-purpose analyses when considering the impact of interacting cracks on a material's lifetime [*Wiesner et al.*, 2000]. SIFs have also been used in geological models to predict fracture behaviour [*Renshaw and Pollard*, 1994; *Olson*, 2004; *Philip et al.*, 2005; *Paluszny and Zimmerman*, 2013] but have not been routinely adopted for investigating geological fracture interaction.

Kachanov [1987] presented an approximate method for calculating how the SIFs of one fracture are affected by another fracture. The system is simplified by using a transmission factor which depends on the fracture geometry and orientation of the stress field, but not the magnitude of the stresses. The 3D formulation of this method incorporates the idea that fracture interaction may amplify (increase) or shield (decrease) stress locally depending on the geometry. Other early analytical approaches include that of *Fabrikant* [1987], who used an iterative procedure to evaluate each fracture's effect on one another. More recently, work has expanded on these methods to improve accuracy or investigate more complex systems of fractures. *Laures and Kachanov* [1991] extended this analysis to 3D microcrack arrays using the same method as *Kachanov* [1987], focusing on cases where one fracture interacts with a group of smaller fractures. They show that 3D interaction effects are generally weaker than 2D interaction effects. *Gross* [1982] first introduced the method of polynomial expansions of tractions on fractures, providing approximate SIFs for multiple straight cracks. *Benveniste et al.* [1989] used a superposition scheme for which *Kachanov* [1987]'s method is a special case. *Zhan and Wang* [2006] used a first-order average traction method to study the same set of geometries as *Kachanov* [1987].

Numerical methods for calculating SIFs provide a convenient means to study SIF alteration, because any arbitrary fracture geometry can be investigated. In 2D, *Fu et al.* [2012] demonstrated amplification and shielding using the displacement correlation method to find SIFs. *Yan* [2010] investigated the interaction of circular arc cracks in tension. *Fan et al.* [2016] investigated the case of two fractures in compression using the FEM and compared their numerical results to photoelastic and uniaxial compressive experiments. *Legrand and Lazarus* [2015] used a finite perturbation method to study fracture interaction in 2D. Along with SIF perturbations, they studied fracture growth and coalescence, evaluating growth using a fatigue law to govern fracture propagation. *Kamaya* [2008b] used the FEM to study SIF variation along the tips of surface cracks, using the SIF perturbation to accurately predict growth [*Kamaya*, 2008a]. Most of these studies investigate interaction of static geometries and yield interaction relationships that depend either on distance or on relative spatial and geometric arrangements, but are restricted to specific geometries such as coplanar or stacked configurations. To aid in interpretation of fracture interaction and growth, there is need for methods which can simulate interaction in full 3D space, without constraining the size, orientation or number of fractures. A flexible numerical approach can be readily applied to any fracture geometry, subjected to arbitrary boundary

conditions, while analytical and semi-analytical approaches may be constrained to specific geometries and conditions.

With the development of advanced 3D FEM based models for studying fracture propagation, SIF-based analysis can be applied to fracture interaction in order to understand the importance of relative fracture spacing. In the present work, a fracture mechanics based 3D FEM model, outlined by *Paluszny and Zimmerman* [2011, 2013], is used to investigate fracture interaction. Advances in methods for FEM SIF computation provide highly accurate results for closely interacting fractures, in particular, by solving for the interaction integral using a disk-shaped domain integral method [*Nejati et al.*, 2015a], without requiring any special mesh structure around the fracture tips. The present work extends the analysis of fracture interaction by investigating changes in the SIFs for all modes of fracture tip deformation, namely modes I, II, and III. Characterisation of interaction is captured by three novel measures for quantifying the spatial distribution of fracture growth energy. Interaction is quantified based on the perturbation of the SIFs by comparing interacting fractures to undisturbed single fractures in the same stress field. The spatial variation of these interaction measures are proposed as 'interaction maps', or 'stress intensity factor variation maps', used interchangeably in this manuscript. These maps provide a new way to assess the extent and magnitude of fracture interaction.

2 Numerical method

The fracture modelling workflow is summarised in four steps: geometry, meshing, deformation and SIF computation. In this work, propagation of fractures is not explored; instead, the focus is on understanding how interaction between fractures enhances or suppresses growth as a function of spatial arrangement. The finite element based fracture mechanics framework used herein is previously detailed by *Paluszny and Zimmerman* [2013], and has been validated for both 2D and 3D geometries [*Paluszny and Matthäi*, 2009; *Paluszny and Zimmerman*, 2011]. The fracture geometry is stored independently of the mesh, and so the mesh is merely an instrument which is used and disposed at each step, created to satisfy both geometric and solution field constraints of the particular simulation stage.

Fractures are represented as smooth surfaces growing in response to tension or compression, governed by the mechanics of brittle failure. The volume is discretised using a volumetric mesh. An initial fracture geometry is created inside a volumetric box representing the rock mass. Fractures can be assigned any surface shape, including non-planar geometries. In this work, fractures are assumed to be disk shaped to simplify analysis, but all methods proposed are also effective for fractures of any shape, provided the shape can be meshed with a consistent refinement along its tip. At each step, an 'ideal' mesh is constructed for the given geometry. The mesh is composed of two element types: isoparametric quadratic tetrahedra in the volume, and isoparametric quadratic triangles on the fracture surface elements. Triangle and tetrahedral elements around the crack tip are taken to be quarter point elements [*Banks-Sills and Sherman*, 1986], which capture the singularity ensuing at the fracture tip by shifting the mid-side node one quarter towards the fracture tip. These have been found to significantly improve the measured stress intensity factor values in unstructured tetrahedral meshes [*Nejati et al.*, 2015b]. In addition, the created mesh is refined near the fracture tip to improve sampling of the displacement field. This refinement is a function of the geometric discretisation of the fracture tip. Automatic re-meshing enables many different fracture geometries to be tested without human interaction.

The FEM approximates the deformation field numerically, as a function of stresses, material properties and geometry, and ensuing stress and strains are derived assuming that the matrix is homogeneous, isotropic, and linear elastic. Stress and strain are governed by

$$\sigma = D(\varepsilon - \varepsilon_0) + \sigma_0 \tag{1}$$

where σ is the Cauchy stress tensor, ε is the infinitesimal strain tensor, σ_0 and ε_0 are the initial stress and strain, and D is a linear elastic stiffness matrix [*Cook et al.*, 2007]. For a static system,

$$\underline{\partial}\sigma + F = 0 \tag{2}$$

where $\underline{\partial}$ is the differential matrix operator, and F represents body forces exerted on the object.

2.1 Stress intensity factor computation

After σ and ε are known throughout the volume at element nodes, SIFs are computed at the tips of the fractures in the volume. SIFs quantify the concentrations of stress around the fracture tips, and are decomposed into three modes corresponding to the modes of crack tip deformation: K_I for opening (mode I), K_{II} for in plane shear (mode II) and K_{III} for out-of-plane shearing (mode III). Analytical solutions for SIFs are only available for a small number of fracture geometries, e.g. elliptical and penny shaped cracks [*Kassir and Sih*, 1975; *Rooke and Cartwright*, 1976]. Complex geometries require numerical schemes to compute SIFs at the tips. The values are approximated along the tips of the fractures by sampling the surrounding stress field. This is challenging, due to high stress gradients and singular fields at the tip.

This work evaluates SIFs for all three deformation modes using the *I*-integral, which is an extension of the more famous *J*-integral for evaluating the total energy release rate at the fracture tip [*Rice*, 1968; *Cherepanov*, 1979]. Using the *I*-integral is beneficial as it can be decomposed into individual SIFs for mixed mode problems [*Yau et al.*, 1980; *Nakamura and Parks*, 1988]. The *I*-integral is widely considered one of the most accurate methods for calculating SIFs in 3D [*Walters et al.*, 2005; *Banks-Sills*, 2010; *Bremberg and Faleskog*, 2015]. The method presents a number of challenges which make it difficult to perform on a standard FEM mesh near the crack tip, such as the challenge of integrating over an unstructured mesh, and conversion to a curvilinear coordinate system. These challenges can be mostly overcome by re-sampling the crack tip region and using a disk-shaped domain integral formulation of the *I*-integral, outlined in full by *Nejati et al.* [2015a]. Integral methods have been shown to be valid when the domain includes material changes or discontinuities [*Yu et al.*, 2009], so the disk-shaped domain integral is suitable for study of very close fractures.

This methodology is implemented as part of the Imperial College Geomechanics Toolkit [*Paluszny and Zimmerman*, 2011] which is built upon the Complex Systems Modelling Platform (CSMP++) API [*Geiger et al.*, 2001], and is mainly oriented at computational rock mechanics and the simulation of fracture growth [*Paluszny and Zimmerman*, 2013; *Salimzadeh et al.*, 2017]. The FEM inversion to calculate Equations 1 and 2 is performed by the Fraunhofer SAMG solver [*Stüben*, 2001], and meshes are generated using a commercial octree-based 3D package.

2.2 Validation of domain integral method

The analytical solutions for the SIFs along the tip of an inclined penny shaped fracture under uniform tension are provided by *Kassir and Sih* [1975]:

$$K_I^a = 2\sigma\sqrt{r/\pi}\sin^2\beta \tag{3}$$

$$K_{II}^a = \frac{2\sigma\sqrt{r/\pi}}{2-\nu}\sin^2\beta\cos\theta \tag{4}$$

$$K_{III}^a = \frac{2(1-\nu)\sigma\sqrt{r/\pi}}{2-\nu}\sin 2\beta\cos\theta \tag{5}$$

where K is the stress intensity factor (SIF) with units Pa m$^{1/2}$, I, II and III are the crack tip deformation modes, σ is the applied normal far-field stress, r is the fracture radius, θ

is the angle around the fracture, β is the inclination of the fracture plane relative to the load, and ν is the Poisson's ratio of the medium. K_I is constant around penny shaped fractures of any inclination, and equal to 0 when the fracture is parallel to the direction of stress. K_{II} and K_{III} change sign on either side of the fracture (top and bottom for K_{II} and sides for K_{III}). Figure 1 compares these analytical solutions to the results for a fracture inclined at 45° to the extension direction. The material property values and far-field loads used throughout this work are $\nu = 0.25$, Young's modulus $E = 1$ Pa m$^{-1/2}$, and normal stress $\sigma = 1$ Pa. The results match the analytical solution very well. Small scatter is found on all the modes as a result of the mesh discretisation.
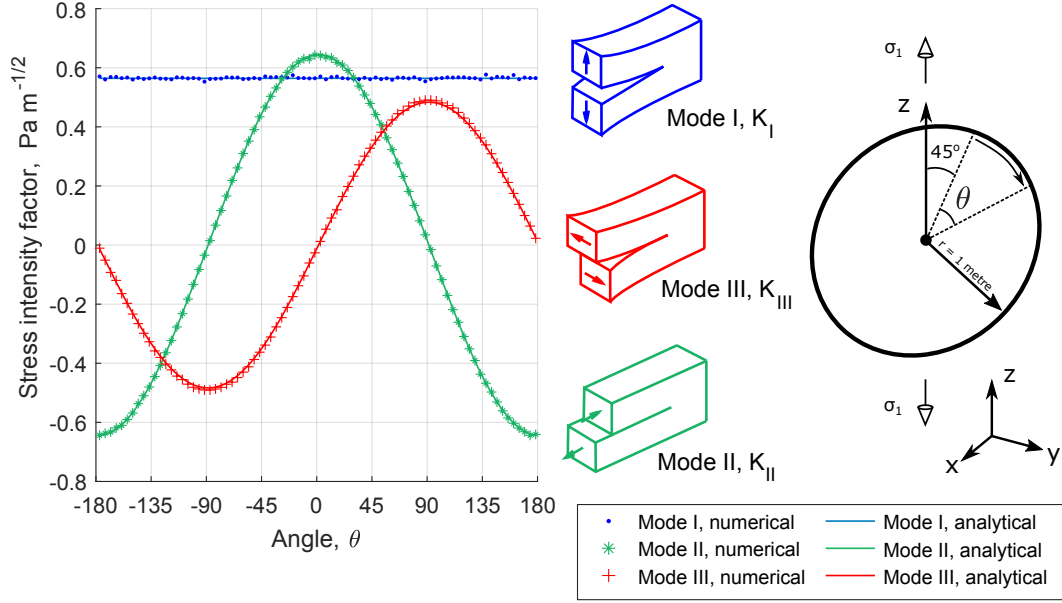

Figure 1. Analytical and numerical stress intensity factors around an isolated fracture. The fracture is in tension, inclined 45° to the stress field. The analytical solution is calculated using Equations 3, 4 and 5. The fracture has 80 tip nodes. The crack tip deformation modes are shown in schematic form to the right of their respective curves.

The total error for all three modes e can be computed as shown by *Nejati et al.* [2015a],

$$e = \frac{\sum_{i=I}^{III} \int_{L_f} \left| K_i^A - K_i^N \right| dl}{\sum_{i=I}^{III} \int_{L_f} \left| K_i^N \right| dl} \qquad (6)$$

where i is one of the three deformation modes (I, II or III), L_f is the fracture circumference, K_i^A is the analytical solution for the mode i SIF, K_i^N is the numerical solution for the mode i SIF, and dl is the distance between fracture tip nodes. Figure 2 shows the variation in e against the number of tip nodes on the fracture, which is used to control mesh refinement. The number of elements in the volume scales linearly with the number of tip nodes. The disk-shaped domain integral method ('disk') is compared to the displacement correlation ('DC') method, another SIF computation method which is more common in the fracture mechanics literature [*Shih et al.*, 1976; *Branco et al.*, 2015]. The results with and without quarter points demonstrate how quarter point elements improve accuracy. The integration radius is set to half the tip length on the fracture, as this produces an accurate result at a good range of refinements. Fracture tip nodes are evenly spaced, so the domain radius can be calculated from the fracture radius.
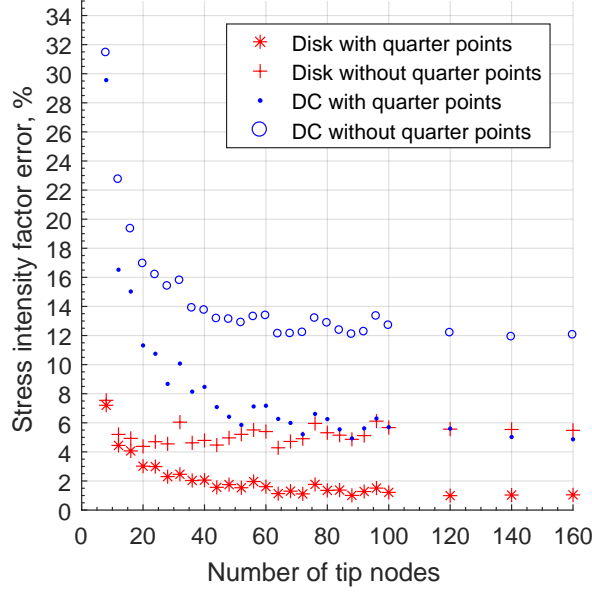
Figure 2. Error in stress intensity factors as mesh size changes. The error, calculated using Equation 6 is shown for a fracture with the same geometry as Figure 1 for different numbers of fracture tip nodes. The number of elements in the mesh (from 8561 to 69816) scales roughly linearly with the number of tip nodes (from 8 to 160) when there is one fracture in the volume.

For higher density meshes, the disk-shaped domain integral technique is shown to be more accurate: the smallest error of 0.9% is found at 120 tips. 80 tips was considered the best balance between accuracy and computation time, with an error of 1%.

3 Stress intensity factor changes due to interaction

The manner in which a pair of fractures interacts is investigated by characterising how SIFs change when two fractures are close. These changes depend on fracture proximity, size, relative position and the type of stress applied, and have been widely observed [*Kachanov*, 1987; *Olson and Pollard*, 1991; *Kamaya*, 2008b; *Fan et al.*, 2016; *Yan*, 2010; *Legrand and Lazarus*, 2015]. The key method of examining interaction, explored by other authors [*Kamaya*, 2008b; *Yu et al.*, 2009; *Legrand and Lazarus*, 2015], is to first calculate the SIFs around a fracture that is interacting with others (K_i^{int}). Then, all but one of the fractures from the domain are removed, and SIFs are calculated for that isolated fracture (K_i^{iso}). In this way, the same geometry for one fracture is tested twice, and the changes in the SIFs can be examined through the ratio between K_i^{int} and K_i^{iso}. The two different fracture domains will have different meshes, but their tip nodes are in the same locations for both calculations, and the mesh around each fracture has a similar structure. The fracture spacing convention introduced by *Kachanov and Laures* [1989] is used in this work, where the spacing is scaled by the fracture radius and reported in the form $\Delta/2r$.

In this work, it is assumed that any difference between K_i^{int} and K_i^{iso} is due to interaction effects. However, both K_i^{int} and K_i^{iso} will be subject to discretisation errors, creating additional small differences. By using a numerical result with the same local mesh around the fracture, similar magnitude discretisation errors at are present each tip in both K_i^{int} and K_i^{iso}. Therefore, the ratio K_i^{int} and K_i^{iso} calculated at each pair of tips factors out these errors. Whilst replacing K_i^{iso} with an analytical solution reduces the number of

terms which contain numerical error, this would compound discretisation errors along with SIF perturbations. Additionally, analytical solutions for isolated SIFs are only available for specific geometries and boundary conditions, whereas fractures can be simulated numerically for any orientation.

3.1 Interaction compared to other methods

No exact analytical solution is available for the change in SIFs due to interaction. Instead, results can be compared to the perturbations found through other semi-analytical or numerical methods [*Legrand and Lazarus*, 2015]. The first method for comparison is *Kachanov and Laures* [1989], whose results provide an approximate solution that closely match other semi-analytical methods for calculating SIFs for interacting fractures [*Fabrikant*, 1987; *Gross*, 1982]. The second method utilises the results of *Legrand and Lazarus* [2015], obtained using the finite perturbation method.

Figure 3 shows the SIF perturbation quantified through the ratio K_i^{int}/K_i^A, obtained using these two methods, and the present method, for a fracture under tension when a second coplanar fracture is nearby. The fractures are oriented perpendicular to the stress field, and are shown for two separations, $\Delta/2r = 0.05$, and $\Delta/2r = 0.00025$. Both fractures have 160 tip nodes. At $\theta = 0°$, where the two fractures are closest together, K_i^{int} is higher than K_i^A as a result of interaction. At the $\Delta/2r = 0.05$ separation, $K_i^{int}/K_i^A = 1.3$, and decreases as the angle increases around the fracture. At separation $\Delta/2r = 0.00025$, K_i^{int} is significantly higher, and $K_i^{int}/K_i^A = 3.2$. K_i^{int} decreases at a much faster rate with angle at the close separation. At $\theta = 60°$, both separations converge to similar values of K_i^{int}/K_i^A. At $160°$, the far side of the fracture is almost unchanged by interaction, yielding values very close to the isolated solution.

All three methods yield a very similar trend. The present simulation results match those of *Kachanov and Laures* [1989] particularly well, except for the low separation case where the fractures are very close ($\theta < 20°$). In this region, the present simulation results have higher K_i^{int}/K_i^A and match *Legrand and Lazarus* [2015]'s results closely. $\Delta/2r = 0.00025$ is a particularly challenging case to discretise, because the region between the fractures becomes very small relative to the fracture size. To place sufficient elements in this region requires an unreasonably high mesh density. Discretised methods that rely on sampling of this region produce scattered SIF values where the fractures are close, which can be seen in Figure 3 for the $\Delta/2r = 0.00025$ case. Similar scatter was reported by *Legrand and Lazarus* [2015] for $\Delta/2r < 10^{-4}$.

Figure 4 shows an example mesh used in Figure 3 with 30 tips and $\Delta/2r = 0.05$, with two fractures in the model to demonstrate the way refinement is focused on the fracture tip.

### 3.2 SIF perturbations for common geometries

Figure 5 shows K_I^{int}/K_I^{iso} for six fracture pairs in two geometries to demonstrate how the magnitude and sign of the interaction changes as the fracture orientation changes. The top row (a-c) shows coplanar interaction where mode I is amplified along the closest part of the fracture. As the separation between fractures increases, K_i^{int}/K_i^{iso} is much lower, becoming effectively equal to unity at $\Delta/2r = 1.50$. The bottom row (d-f) show a stacked configuration where mode I is uniformly shielded as a result of interaction. This effect is diminished with increasing separation, but could be said to have a larger range than the coplanar geometry, because, at $\Delta/2r = 1.50$, mode I is still reduced, as observed by other analyses of stacked cases [*Kachanov*, 1993]. In the stacked configuration, mode II varies in a similar but opposite manner to mode I, where it is amplified rather than shielded. Mode II is perturbed uniformly all the way around the fracture, because the fracture tips are all the same distance from the interacting fracture.

(a)

(b)
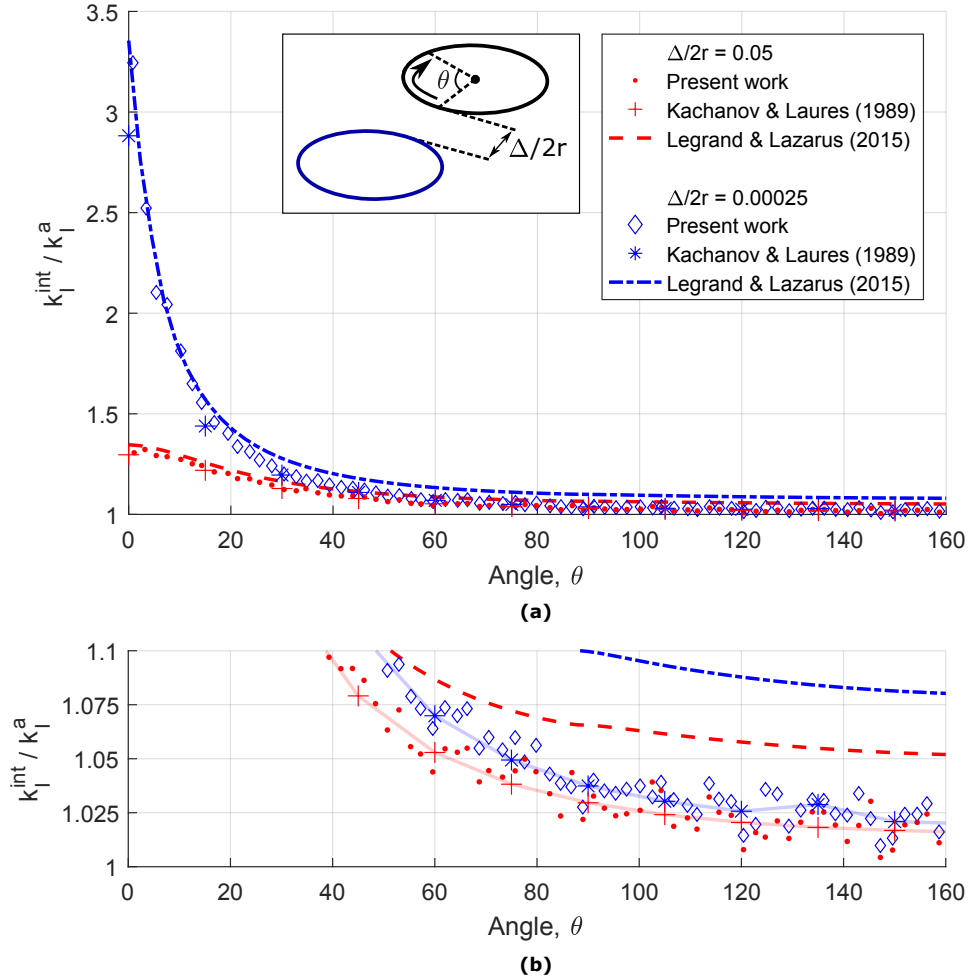
Figure 3. Comparison of stress intensity factor perturbations with other models. (a) SIF ratio between the interacting and isolated fractures (K_i^{int}/K_i^A). The fractures are perpendicular to the stress field and are plotted for two separations ($\Delta/2r = 0.05$, and $\Delta/2r = 0.00025$). Both fractures have 160 tip nodes. Results by *Kachanov and Laures* [1989] and *Legrand and Lazarus* [2015] are provided for the same geometry. (b) The same data from (a), but with the y-axis limits changed to (1.0-1.1). Lines have been placed to connect *Kachanov and Laures* [1989]'s points for ease of visualisation.

Coplanar and stacked geometries are the 'end member' cases for fracture interaction, where pure amplification and pure shielding take place, respectively. The transition between these cases is the overlapped case, where part of the fracture is shielded and part is amplified. As the fractures move from coplanar to stacked, the mode I SIF change becomes negative at the point where the fractures are overlapped, and positive where they do not overlap. Mode II and III SIFs also change their perturbation behaviour across this transition, giving rise to the changes in growth angle which are well known to occur as fracture offset changes [*Thomas and Pollard*, 1993]. This behaviour, whilst intuitive for many applications of fracture mechanics, can be quantified and better understood through further analysis of SIF perturbations. Moreover, the relative orientation of the fractures will further affect the manner in which interaction takes place (see Section 5).
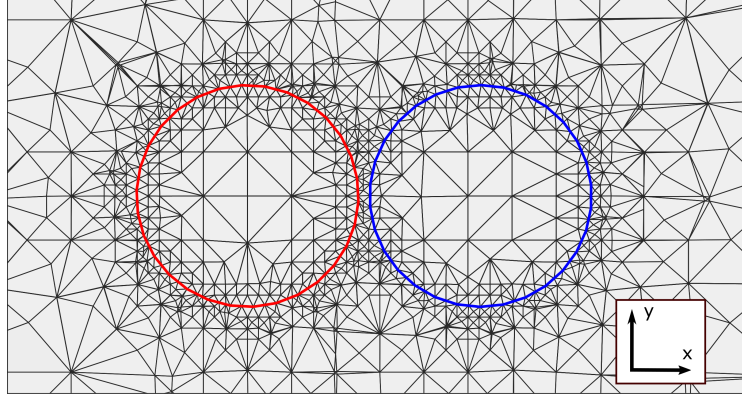
Figure 4. Example mesh around two fractures with separation $\Delta/2r = 0.05$. Each fracture has 30 tip nodes. Volumetric elements are cut by the visualisation plane, so some appear to be thin an elongated, whereas they actually pertain to a well formed tetrahedral element.

4 Quantification of interaction

4.1 Measures of interaction

In this section, several measures are proposed to quantify and characterise interaction. These 'measures of interaction' derive from simple relationships similar to K_i^{int}/K_i^{iso}. Whilst the ratio K_i^{int}/K_i^{iso} is powerful on its own, it cannot be expanded to modes II and III for tension, as these modes change sign around the fracture, *e.g.* Figure 1 . Therefore, use of K_i^{iso} in the denominator should be avoided, as it approaches zero for certain angles. The same is true for mode I in certain fracture orientations or stress states. Additionally, K_i^{int}/K_i^{iso} is also only measured on individual tips, with many values per fracture.

It would be useful to have a single quantity that captures how a fracture is changed due to interaction. Summarising interaction with one value enables analysis using interaction variation maps, aiding understanding of past and potentially arising fracture geometries. For simulations containing hundreds and thousands of fractures, cheap and local measures of interaction will aid the discretisation and level of detail required at different locations of the mesh. The methods proposed herein for characterising interaction are effective for all deformation modes and boundary conditions.

Three such methods are proposed as follows. The first, 'circumferential SIF perturbation', computes the total area between the K_i^{int} and K_i^{iso} curves, either as as sum of all modes (C) or for one specific mode (C_i). The second, 'maximum SIF perturbation' (M_i), computes the maximum perturbation of K_i for the fracture. Both of these methods are used to quantify the magnitude of the interaction. The third, ϵ, the 'amplification to shielding ratio', quantifies whether the fracture is mostly amplified or shielded. Using either C or M_i along with ϵ captures the change in the SIFs at its tips as a result of nearby fractures.

4.1.1 Definition of circumferential SIF perturbation, C

Circumferential SIF perturbation is defined as the absolute area between the interacting and isolated SIF curves, as a modification of Equation 6, as follows:

$$C = \frac{\sum_{i=I}^{III} \int_{L_f} \left| K_i^{iso} - K_i^{int} \right| dl}{\sum_{i=I}^{III} \int_{L_f} \left| K_i^{iso} \right| dl} \tag{7}$$
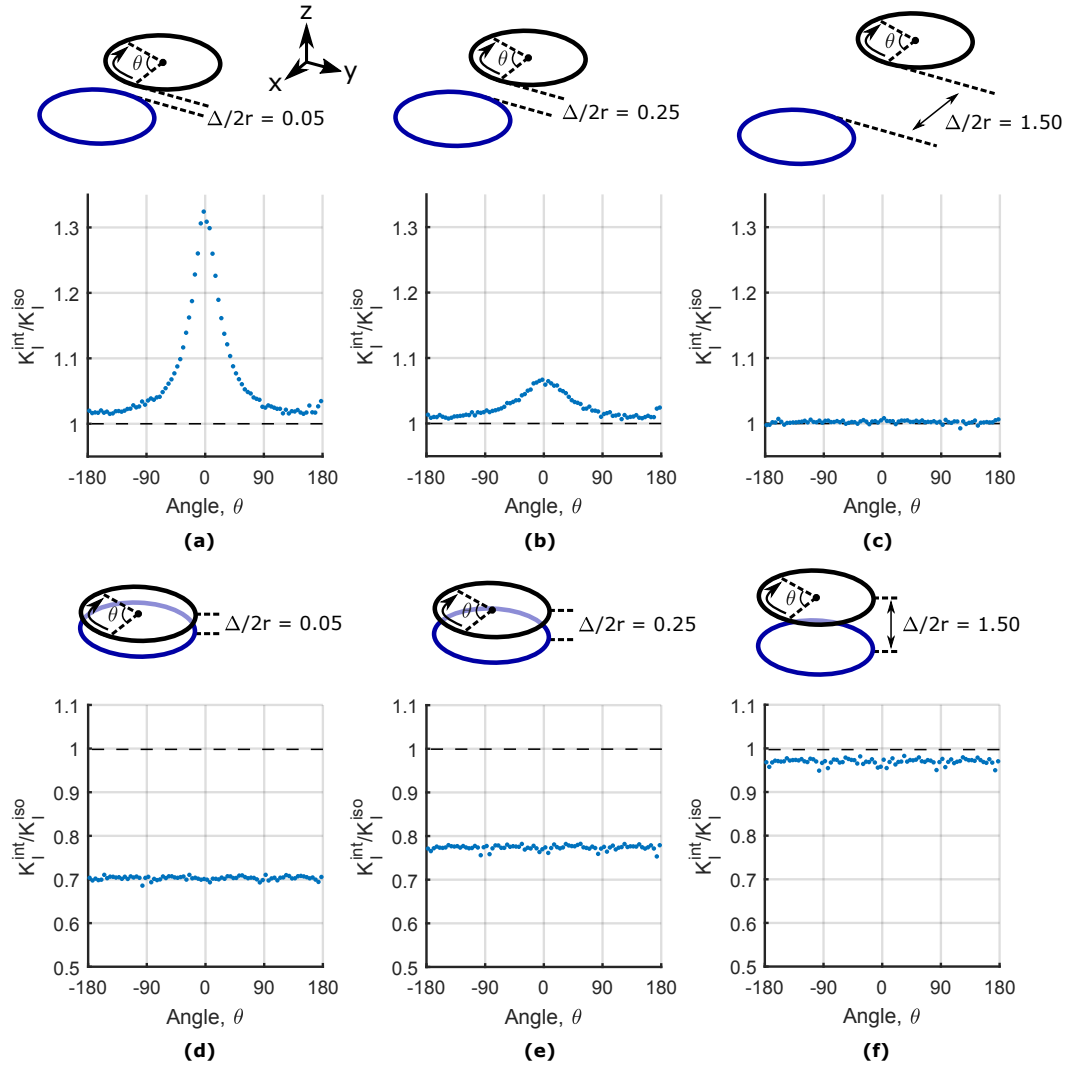
Figure 5. Change in mode I stress intensity factor resulting from close fracture interaction. (a), (b) and (c) show the case where two fractures are coplanar, *i.e.* on the same x plane, with changing separation along the y axis. At $\theta = 0$, the two fractures are closest to one another, and K_I is amplified. (d), (e) and (f) show a stacked configuration, *i.e.* moving up the z axis. The change in the mode I SIF is represented using K_I^{int}/K_I^{iso}. The dashed line in each graph shows the isolated result that would occur if the fractures were isolated, where $K_I^{int}/K_I^{iso} = 1$.

where K_i^A is replaced with the SIF for an isolated fracture, K_i^{iso}. K_i^N becomes the SIFs for an interacting fracture, K_i^{int}. This provides a value that represents how much more concentrated stress has become at its tip as a result of other nearby fractures.

As C is a sum over the entire fracture, it is not directional, *i.e.* it does not identify where the fracture may fail, but instead represents the total interaction a fracture undergoes, which may be the result of more than one interacting fracture. C should also be considered a non-local measure. Because the same tip node locations can be used to calculate K_i^{iso} and K_i^{int}, additional errors caused by mesh discretisation can be minimized. C can also be calculated for just one mode of deformation (i) rather than the total sum of all

modes,

$$C_i = \frac{\int_{L_f} \left| K_i^{iso} - K_i^{int} \right| dl}{\int_{L_f} \left| K_i^{iso} \right| dl}, i = I, II, III. \tag{8}$$

This is useful for calculating how one individual mode is altered by interaction. The use of absolute values for C in the denominator avoids asymptotes when the SIFs are very close to 0.

4.1.2 Definition of maximum SIF perturbation, M_i

Maximum SIF perturbation is defined as the largest difference between the interacting and isolated SIFs,

$$M_i = \max \left(\left| K_i^{int} - K_i^{iso} \right| \right), i = I, II, III. \tag{9}$$

This measure can be related to one specific location on the fracture tip at which the difference was largest. This makes M_i a local measure of fracture interaction. The maximum SIF perturbation is unique between the three deformation modes, as the tip node with the maximum M_I is not necessarily the same as the tip node with maximum M_{II} or M_{III}. The magnitude of M_i is tied to σ. As the method relies on the value of one particular tip, rather than averaging over a group of tips, it may be subject to greater discretisation errors.

An illustration of the differences between C and M_i is shown in Figure 6(a). This plots the mode I SIF as a function of the tip angle in the same manner as Figure 1. The shaded region shows the area between the interacting and isolated curves (C_I), and M_I is shown as the maximum change. Both C and M_i use the absolute values of K_i^{int} and K_i^{iso} in their calculations. Thus, they only provide information on the magnitude of interaction, and not whether it is amplifying or shielding.
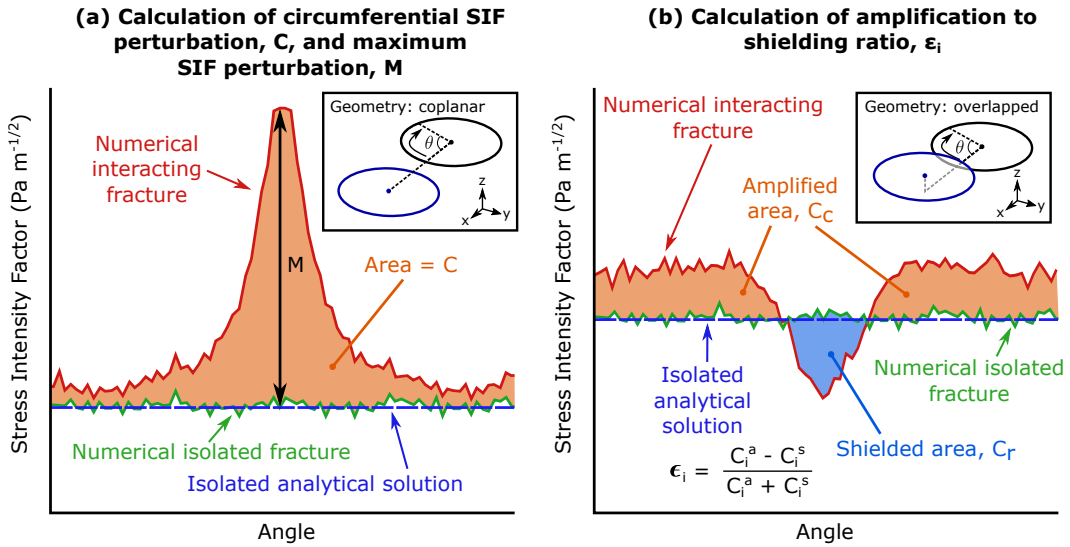
Figure 6. Methods used to quantify fracture interaction by calculation of C, M_i, and ϵ. (a) shows C as the area between the two numerically calculated SIF curves for the same coplanar geometry, one isolated and the other interacting with other fractures. M is the maximum difference between the two curves. (b) shows the SIFs for an overlapped fracture geometry, and the calculation of ϵ_i by comparing the area of the graph that is amplified to the area that is shielded.

4.1.3 Definition of the amplification to shielding ratio, ϵ_i

When measuring interaction, it is important to consider whether stress has been amplified or shielded. In the simple cases of coplanar interaction, stress is only amplified, *e.g.* Figure 5(a-c). In cases where the fractures are stacked and at least partially overlap, stress is shielded, *e.g.* Figure 5(d-f). The type of interaction, either shielding, amplification, or a mixture of the two, is quantified by the amplification to shielding ratio (ϵ_i), which is formulated as follows. Two lists of values, κ_i^a and κ_i^s, are created from the difference between the interacting and isolated SIFs. κ_i^a, contains the values where the SIFs for mode i have been increased, and 0 otherwise,

$$\kappa_i^a = \begin{cases} K_i^{int} - K_i^{iso} > 0, & \kappa_i^a = K_i^{int} - K_i^{iso} \\ K_i^{int} - K_i^{iso} \leq 0, & \kappa_i^a = 0 \end{cases} \tag{10}$$

and κ_i^s contains values where the SIFs for mode i have been decreased, and 0 otherwise,

$$\kappa_i^s = \begin{cases} K_i^{int} - K_i^{iso} > 0, & \kappa_i^s = 0 \\ K_i^{int} - K_i^{iso} \leq 0, & \kappa_i^s = K_i^{int} - K_i^{iso}. \end{cases} \tag{11}$$

These lists therefore contain information for the tips which have been only amplified (κ_i^a) and only shielded (κ_i^s). The areas under the curves of κ_i^a and κ_i^s are then calculated:

$$C_i^a = \int_{L_f} |\kappa_i^a| dl, \tag{12}$$

$$C_i^s = \int_{L_f} |\kappa_i^s| dl. \tag{13}$$

The balance between amplification and shielding can be found by comparing these two areas. Thus, ϵ_i is defined as

$$\epsilon_i = \frac{C_i^a - C_i^s}{C_i^a + C_i^s}, i = I, II, III. \tag{14}$$

Therefore, ϵ_i equals 1 when mode i is purely amplified, and equals -1 when purely shielded. When $\epsilon_i > 0$, the SIFs at most of the tips of the fracture are amplified by the presence of another fracture, and when $\epsilon_i < 0$, most of the tips are shielded.
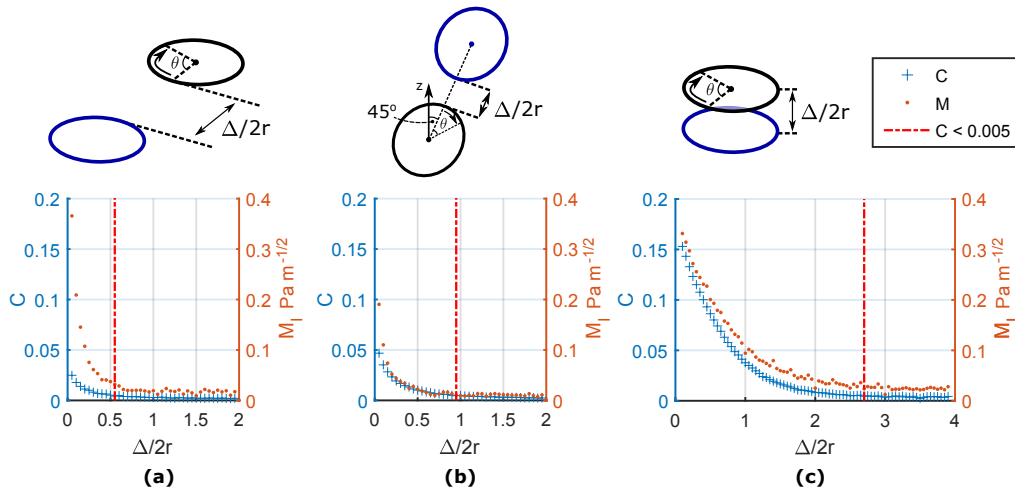
4.1.4 Comments on interaction measures

Numerical simulations inevitably produce different results when changes are made in the domain, even if those changes are slight, due to discretisation and numerical errors, as discussed in Section 3. This means that there will always be differences between K_i^{iso} and K_i^{int}, even when the meshes are identical and fractures are very far apart. Therefore, the measures of magnitude (C and M) do not converge to zero when fractures do not interact, but do become very small. This is not a problem for analysis of C and M_i, because the size of this error is small compared to cases when interaction is significant. However, scatter between the values of K_i^{iso} and K_i^{int} will result in ϵ_i being essentially random. When analysing a set of ϵ_i values in space, a threshold should be used to ignore the value of ϵ_i if either C_i or M_i suggests there is very little interaction. Conveniently, C_i has the same magnitude regardless of the SIF magnitude because it compares the ratio of two areas. A threshold of $C_i = 0.005$ is used in this work.

The proposed interactivity measures share some commonalities with the transmission factor used as part of *Kachanov* [1987]'s analytical method. For coplanar fractures, the transmission factor is increased by the presence of the other fracture. In 3D, the sign of the transmission factor changes to correspond to cases of fracture interaction either amplifying or shielding stress depending on the geometry. For fracture arrays, the transmission factor concept is extended to an interaction matrix, containing transmission factors which

describe the effect of each fracture on one another. The interaction measures suggested here are similar, but are now separated into magnitude and sign of interaction, where C or M_i can be used to show the magnitude of interaction, and ϵ_i describes the balance of amplification or shielding. These measures are also assigned one per fracture, rather than one per fracture pair.

4.2 Variation of C and M with separation

Figure 7 shows how C and M_I vary in the simple case of increasing fracture separation for three geometries. C is used rather than C_I to highlight the effect of combining the three modes together. All graphs (a-c) use the same axes, with C on the left and M_I on the right. In all three geometries, C and M_I demonstrate how interaction reduces with separation. Both interaction measures show that shielding interaction when fractures are stacked (c) has a larger range than coplanar geometries, (a) and (b). The separation at which C falls below 0.005 is marked with a red dashed line, showing that shielding effects have a much longer range than amplification effects.


Figure 7. Variation of C and M_I with fracture separation for three common geometries as a function of increasing fracture separation. In order to highlight the effect of combining modes together in interaction measures, C is compared to M_I here. (a) Coplanar geometry, also examined in Figure 5(a-c). (b) Inclined coplanar geometry. (c) Staked geometry, also examined in Figure 5(d-f). Fracture separation is measured in terms of $\Delta/2r$, where r is the fracture radius. The dashed red line marks the smallest $\Delta/2r$ where $C < 0.005$, the threshold at which there is considered to be no significant interaction. This is reached at $\Delta/2r = 0.55$ in (a), $\Delta/2r = 0.95$ in (b), and $\Delta/2r = 2.70$ in (c).

For the same separation variation of two fractures, their interaction is shown to not only depend on their spacing, but also on their relative positioning with respect to the far-field stresses and their relative positioning with respect to one another. The difference in the behaviour of C and M_I in each case is of particular interest, especially when comparing the two coplanar cases. In Figure 7(a), only mode I is changed by interaction, because the fractures are perpendicular to the stress field and K_{II} and K_{III} are zero. Figure 7(b) has the same geometry, but is oriented at 45° to the stress, meaning modes II and III are non-zero and are perturbed by the interaction. M_I only relies on mode I, so is higher in (a) where the interaction is confined to one mode, and smaller in (b), when the interaction is shared by three modes. C is the sum of the SIF perturbation for all three modes, so has a higher magnitude in (b) than in (a). Discretisation errors cause small amounts of scatter, and are much higher in M_I than C.

–14–

In summary, C and M_i are both capable of capturing the decrease in interaction with separation, however, care should be taken to examine which modes are being altered in each case. Separating C into its mode specific values C_I, C_{II} and C_{III} to summarise the change in each mode, using Equation 8, may be preferable during interaction analysis, in order to identify where fractures will become non-planar during growth [*Thomas and Pollard*, 1993].

For numerically derived values to be useful for analysis, they must not vary strongly as a function of mesh refinement. Figure 8 shows, for two fractures with $\Delta/2r = 0.25$, the value of C and M_I, plotted against the number of tip nodes on the fracture, similar to Figure 2. Changes in separation have a much larger effect on C and M_I than changes in mesh density. The standard deviation of C and M_I across 27 meshes are 0.00038 and 0.0023 respectively. M_I varies more as it is reliant on the value from one node rather than an average across all nodes.
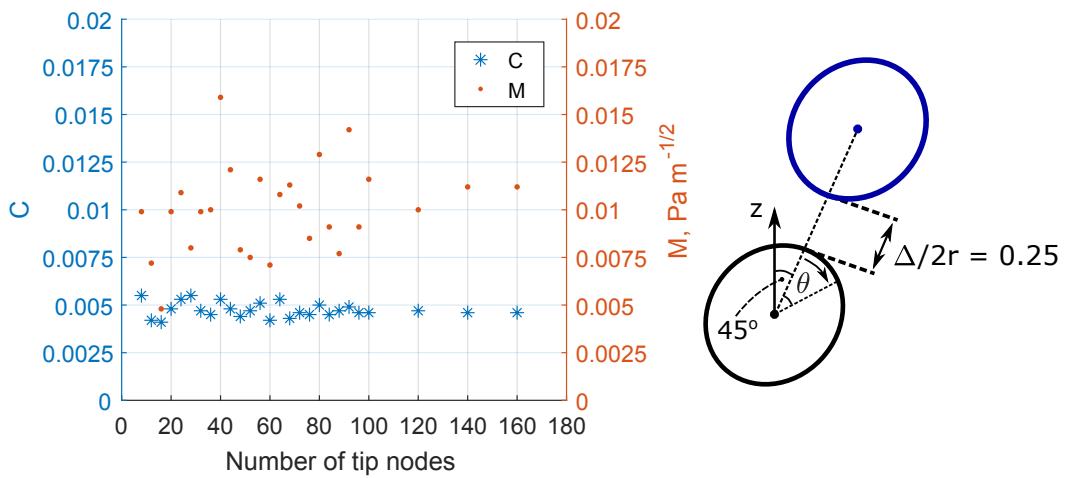

Figure 8. Sensitivity of interaction measures to mesh refinement. Two fractures have been placed with separation $\Delta/2r = 0.25$ on the same plane inclined 45° to the z axis. C and M_I are measured on one fracture for different mesh refinements, where the density of the mesh is controlled by the number of tips around the fracture.

5 Interaction maps

In this section, fracture interaction maps are constructed to analyse the effect of one fracture on another, specifically by capturing SIF variations comprising multiple interaction cases, within a single image. They show the variation of C_i, M_i and ϵ_i as the relative position between two fractures changes. A fracture interaction map is constructed by performing simulations in which a base fracture is placed in a fixed position, perpendicular to the direction of stress. A second fracture of equal radius is placed nearby with the same orientation. The values of C_{I-III}, M_{I-III}, and ϵ_{I-III} are then measured on the base fracture in tension. The second fracture is then moved to other locations and the same measurements were made. This creates a grid of values in the x, z plane around the fracture, which is interpolated to create a continuous map of SIF variation around a static fracture. Figure 9 demonstrates this process for three locations alongside the fracture interaction map for ϵ_I.

The objective of creating an interaction variation map is to explore the variation of the magnitude and type of interaction, *i.e.* amplification, shielding, or a mix of the two,
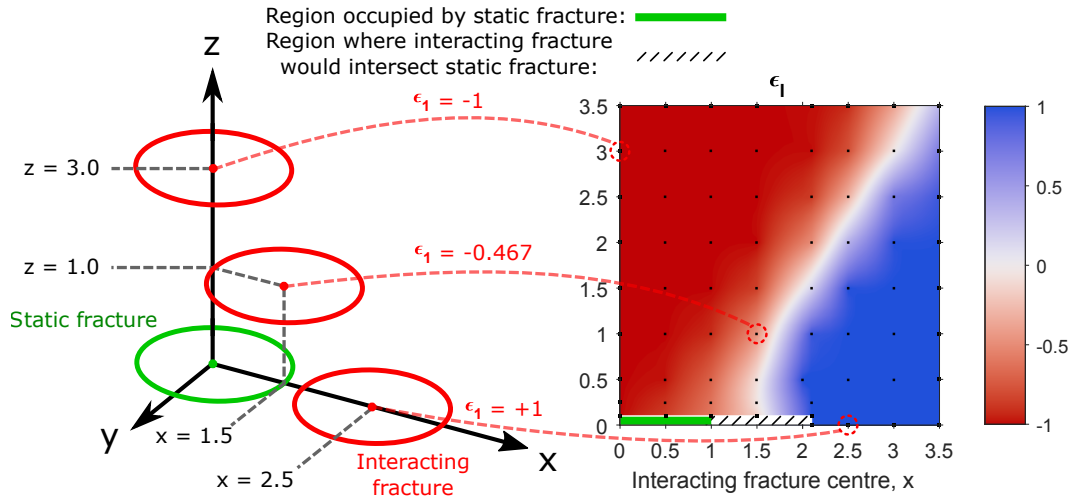
Figure 9. Schematic demonstrating creation of stress intensity factor variation maps. Maps are built up of the results of many simulations. In each simulation, only two fractures are present at one time: the static fracture (green) remains centered at $(0, 0, 0)$ and the interacting fracture moves around the $x > 0, z > 0$ quadrant. The dashed space in the plot shows the region which cannot be sampled, because in this region the fractures intersect. This region changes size based on the orientation and offset of the interacting fracture. An interaction measure (C_{I-III}, M_{I-III}, and ϵ_{I-III}) is measured on the static fracture, and then is interpolated over the sampled space.

depending on relative fracture position and orientation. Compared to plotting the change in stress around a fracture (*e.g. Grechka and Kachanov* [2006]), interaction maps observe the change in the SIFs. Therefore, the impact of interaction is more directly quantified in terms of changes at the fracture tip, and can be examined separately in modes I, II and III. This process could be used to create interaction maps of any interacting fracture orientation or size, as long as the sampled locations do not cause fractures to intersect.

Fracture interaction variation maps are presented in Figures 10, 11 and 12 showing values of C_{I-III}, M_{I-III}, and ϵ_{I-III} respectively. Each Figure includes maps for two orientations of the interacting fracture. (a) shows the interaction map generated from two fractures inclined perpendicular to the direction of tension, and (b) shows the map with the interacting fracture inclined 45° towards the other fracture.

5.1 Interaction variation maps of C_i

Figure 10 shows fracture interaction maps of C_I, C_{II} and C_{III} for two geometries. The coplanar geometry (a) shows the gradual change between coplanar and stacked geometries. The magnitude of the interaction in the stacked configuration, along $x = 0$ as shown in Figure 7(c), was shown to be higher than in the coplanar configuration, along $z = 0$, as shown in Figure 7(a) and (c). This behaviour is clear on the interaction variation map of C_I, where the extent of the highly perturbed region is much larger when the fractures overlap and enter one another's stress shadow.

In Figure 10(a), C_I shows that mode I is the most perturbed interaction mode, particularly when fractures are overlapping. Mode II and III are perturbed at approximately half the magnitude of mode I. Mode II perturbations are not increased uniformly in the overlap region. This is because mode II tends to be perturbed only where fracture tips are close to one another. Otherwise, mode II relatively unperturbed if the tip lies above the fracture surface. This leads to larger magnitudes when more of the fracture tips are lined

up vertically, creating a region of lower C_{II} between $x = 0.5 - 1$. These changes in C_{II} highlight where fractures will undergo non-planar growth as a result of interaction, due to increased mangitudes K_{II} [*Cotterell and Rice*, 1980], as observed in én echelon fracture sets [*Delaney and Pollard*, 1981]. Mode III is most perturbed when the fractures are partially overlapped, and is unperturbed when the tips are close together. This results in its highest value being in the region of $x = 1$, $z = 0.5$. Outside of this overlapped region, C_{III} is essentially unperturbed, *i.e.* it falls below the 0.005 threshold discussed in Section 4.1.4.

The inclined geometry in Figure 10(b) show much lower magnitudes of C. This is partially because the fracture surfaces cannot be placed exactly next to one another, so the highly interacting stacked case cannot be produced at any interacting fracture location. Regions where mode I is more strongly perturbed are present when interacting fracture's tip is very close to the base fracture plane. In the same manner as in the coplanar case, mode II is larger when the fracture tips are close and overlap in (b), creating a trough along the line $z = 0.75$ for the 45° inclination.
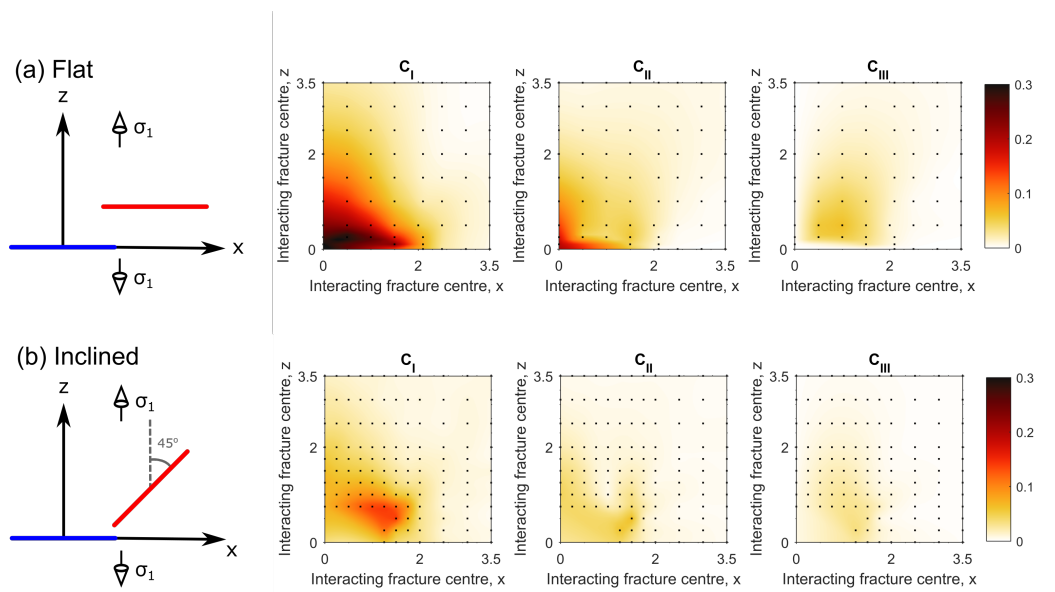
5.2 Interaction variation maps of M_i

The interaction maps of M_i in Figure 11 show that M_i changes in a similar manner to C_i, particularly in (b). The major difference is in the stacked case in Figure 11(a), where the highest M_I is found when fractures are partially overlapped rather than fully stacked. When fractures are partially overlapped, the most significant shielding occurs at the centre of the overlapped tips, resulting in a high value for M_I. When fully overlapped, the shielding is instead uniform around the whole tip, but lower, resulting in an intermediate value for M_I. By measuring the area instead, C_I considers the interaction magnitude to be higher in the fully stacked case and intermediate in the overlapped case, as observed in Figure 7.

5.3 Interaction variation maps of ϵ_i

Figure 12 shows interaction maps that plot ϵ_I, ϵ_{II} and ϵ_{III} for the same geometries as Figure 10. In the coplanar geometry in Figure 12(a) ϵ_I demonstrates the transition between stress amplification and shielding very well. Coplanar orientations result in amplification where $\epsilon_I = 1$, and stacked orientations result in shielding where $\epsilon_I = -1$. The transition zone is well resolved even at the coarse resolution of the grid. ϵ_I is presented without altering values where C_I is below the threshold of interaction because the few locations where it is below 0.005 do not cause the distribution of ϵ_I to be less uniform. The extent of the shielded zone changes significantly in the inclined case in Figure 12(b), demonstrating the impact of fracture orientation on interaction behaviour. When the interacting fracture is inclined at 45°, the extent of the shielded zone is much smaller because the region of stress amplification at the fracture tip is closest to the other fracture. At -45°, the shielded zone is much larger, because the surface of the fractures face one another in this orientation, combining two stress shielding regions. The coplanar non-offset case of ϵ_I in Figure 12(a) can be seen as an intermediate between these two states.

The parameter ϵ_{II} has the most complex distribution of the three modes. In (a), ϵ_{II} is amplified, but a zone of shielding is found on the line $x = 1$ where the fractures are partially overlapped, contrasting the pure amplification when the fractures are fully overlapped. A second small zone of shielding is found when the fractures are very close. These shielding zones also arise in (b). The complex distribution of ϵ_{II} reflects the significant changes to fracture propagation angles when fractures are en échelon, because the fracture growth angle depends on a combination of all three modes. It also corresponds to the region of lower magnitude C_{II} in Figure 10(a).

Figure 10. Stress intensity factor variation maps of C_I, C_{II} and C_{III} for two geometries: coplanar (a) and inclined by 45° (b). Black dots denote sampled points. Larger values of C denote higher magnitudes of SIF perturbation and therefore interaction. Both fractures have a radius of 1 m and 80 tip nodes.
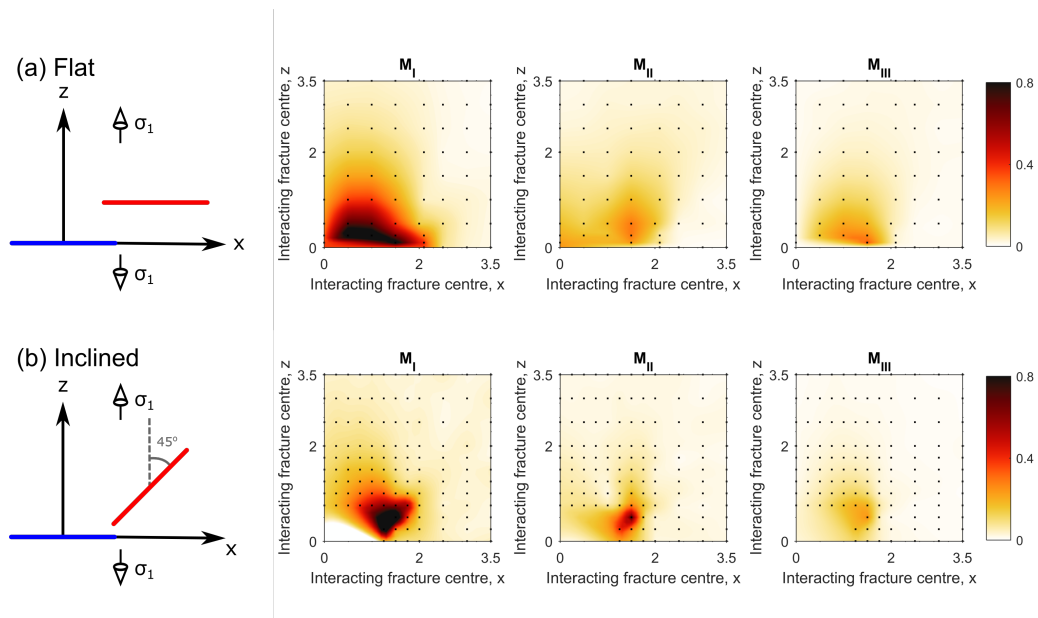
Figure 11. Stress intensity factor variation maps of M_I, M_{II} and M_{III} for two geometries: coplanar (a) and inclined by 45° (b). Black dots denote sampled points. Higher values of M_I, M_{II} and M_{III} show where that mode changed most significantly from their isolated state.
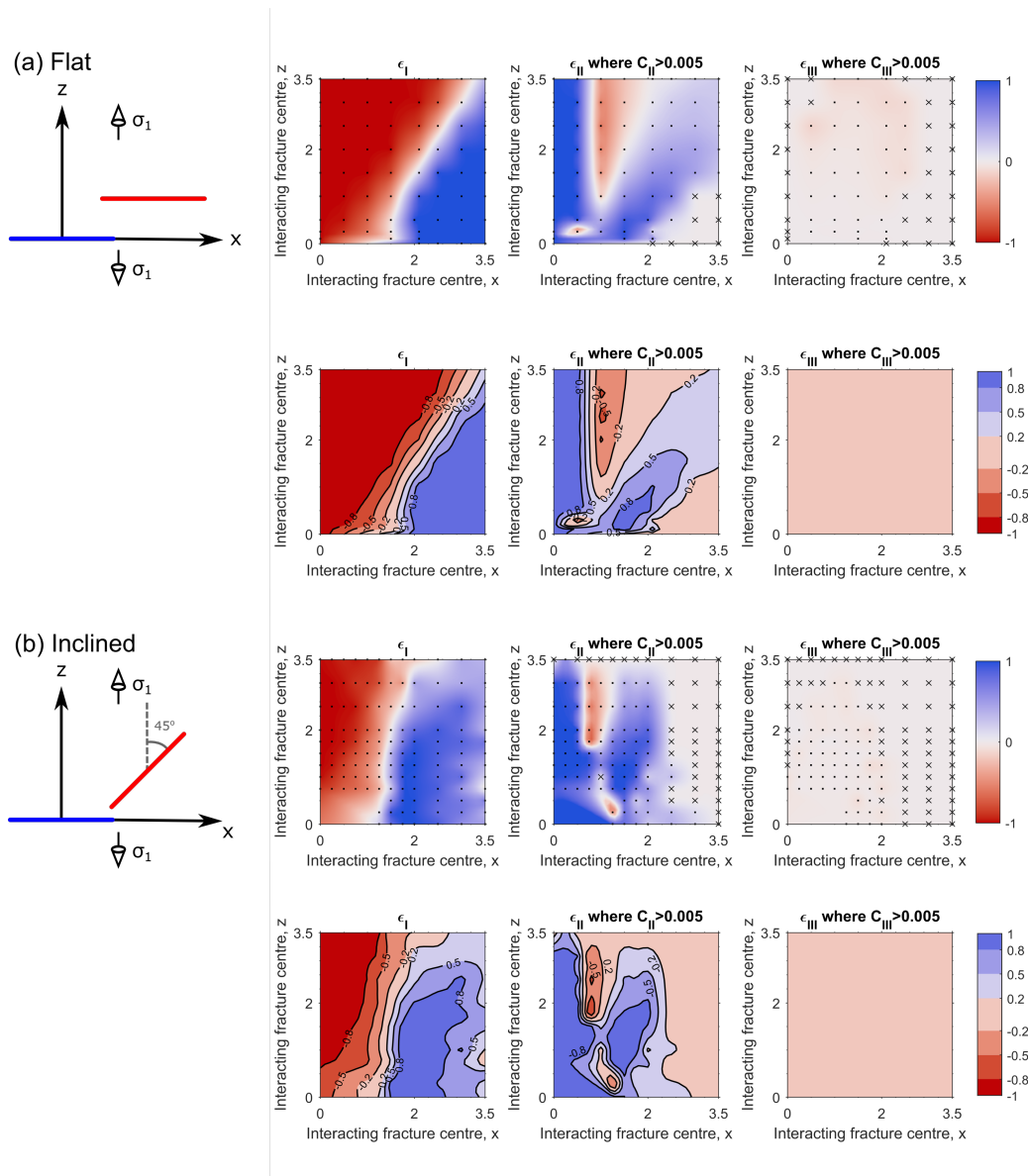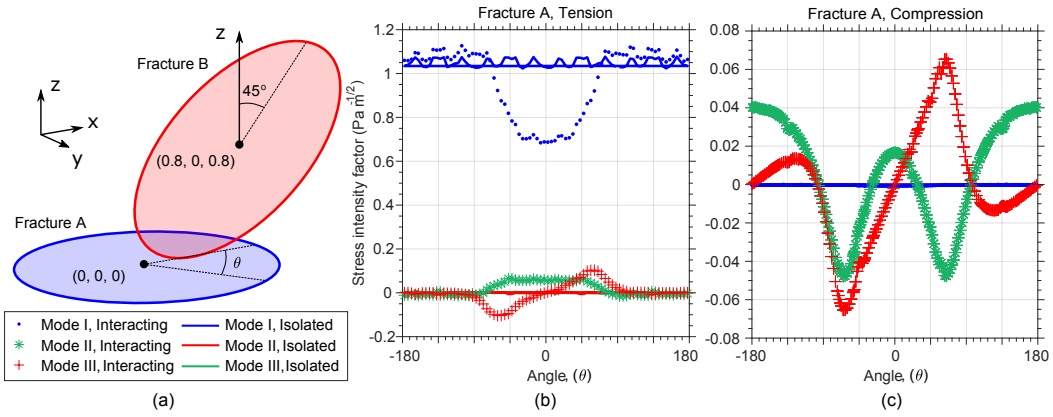
Figure 12. Stress intensity factor variation maps of ϵ_I, ϵ_{II} and ϵ_{III} for two geometries: coplanar (a) and red inclined by 45° (b), in surface and contour format. $\epsilon_I = 1$ denotes that the SIFs around the fracture are amplified all the way around the tip and $\epsilon_I = -1$ denotes that they are shielded. Intermediate values denote that the fracture is partially amplified on one side and shielded on the other. Black dots denote sampled points, and crosses denote points where C_i is less than a threshold amount (0.005). At these points, ϵ_i is set to 0 because ϵ_i produces scattered values when the SIFs in the isolated and interacting cases are very close. Both fractures have a radius of 1 m and 80 tip nodes.

In both geometries there is generally very little variation in ϵ_{III}. Typically, ϵ_{III} is around 0 when the fractures are close (x and $z < 2$), and elsewhere the magnitude of C_{III} is below the threshold (0.005). K_{III} is therefore always equally shielded and amplified if it is altered due to interaction. The threshold of $C_i > 0.005$ is mostly effective at removing misleading values where there is no interaction in modes II and III.

5.4 Comparison between tension and compression

The SIF interaction results in Sections 4 and 5 show results for fractures under tension. When fractures are compressed, friction between the two sides of the fracture perturbs the SIFs [*Liu and Borja*, 2008]. This additional force is important for geological fractures, where compressive stress regimes are common and the surfaces of fractures will have significant roughness, or brecciated material if they are open. In order to incorporate fracture surface friction, the gap-based Augmented-Lagrangian contact resolution method proposed and validated by *Nejati et al.* [2016] is incorporated into the simulation. This approach is specific to accurately resolving the contact and frictional forces between fracture surfaces, using an iterative approach. The method accurately calculates tractions and apertures between the two surfaces that are in contact. Initially, fractures have zero aperture, and the stick or slip condition at each fracture surface node is an emerging property of the simulation. During compression the fractures close, and may either stick or slip, rendering the mode I SIFs negative until contact is resolved.

Figure 13. Geometry of two interacting fractures (a), and the resulting effect on the stress intensity factors for both tension (b) and compression (c). In (c) all modes of SIFs are collapsed to zero for the isolated fracture case. Interaction affects the horizontal fracture in tension, by reducing K_I, and under compression, by inducing non-zero K_{II} and K_{III}, consistent with slipping of the fracture surface. The analytical solution for mode I is also visible as the flat blue line in (b).

The values of SIFs depend on the friction coefficient assumed for the fracture surface. For fracture stick, SIFs are reduced to zero in most cases, as the fracture does not display in-plane deformation. For slip cases, the deformation of the fracture leads to non-zero stress intensity factors. Figure 13 illustrates the behaviour of two interacting fractures under tension and under compression. In the compressive case, the friction coefficient is assumed to be zero, in order to highlight the slip mode, and accentuate interaction. Specific values of C, M_i and ϵ_i for these cases are:

- Tension

    - $C = 0.06$, $C_I = 0.11$, $C_{II} = 0.02$, $C_{III} = 0.03$

- – M_I = 0.35, M_{II} = 0.07, M_{III} = 0.10

- – ϵ_I = -0.65, ϵ_{II} = 0.62, ϵ_{III} = -0.04

- Compression

  - – C = 75.01, C_I = 0.46, C_{II} = 117.11, C_{III} = 107.46

  - – M_I = 0.0004, M_{II} = 0.047815, M_{III} = 0.07

  - – ϵ_I = -0.64, ϵ_{II} = 0.17, ϵ_{III} = -0.009

SIFs are plotted for the horizontal fracture. While in tension KI values dominate under compression KI values are reduced to zero, and K_{II} and K_{III} values become dominating. Interaction can be summarised using the same quantities as before. For tension, values of C, M_i and ϵ are consistent with low interaction. In contrast, under compression, values of C_{II} and C_{III} highlight the effect of the vicinal sliding fracture. In the isolated compression case, SIF values of the isolated fracture case k_i^{iso}, are close to zero. Therefore, the normalised area between SIF curves is much smaller, and the resulting C values are larger. M_i captures accurately the interaction effect between the two fractures, even if the isolated case has very low SIFs. For both tension and compression, M_i yields similar values of interaction between the fractures, with the exception of mode I which is non-interactive in the compression case. It follows that the same variational maps demonstrated in previous sections can be employed to analyse the present case.

6 Discussion

6.1 Geological context

Fracture interaction maps provide a useful method for analysing how a system of fractures will behave. Since the geometry of many fracture systems is well constrained through field and geophysical data, the state of interaction can be explored for a variety of boundary conditions. The interaction measures C and M_i provide a quantitative way to establish whether fractures are interacting, by comparing the values to a threshold, as shown by their change with separation in Figure 7. For the fractures that are considered to be interacting, maps of ϵ_i show whether that interaction will amplify or shield potential growth. This workflow would provide a quantitative assessment for how a network of joints or dykes will behave, for example, during coalescence into a fault, or ahead of the tip of a fault with a damage zone. In particular, the amount of curvature expected when en échelon fracture pairs grow can also be analysed using the interaction maps. Fractures growing when centred in regions where $C_{II,III}$ and $M_{II,III}$ are high will deflect significantly towards the other fracture. These regions arise when the fractures are overlapped, as found in experiments, *e.g. Thomas and Pollard* [1993].

Whilst the methods proposed do not vary with the scale of the fractures being studied, it should be noted that SIFs require that the fractures have distinct tips. Large faults have significant damage zones ahead of their tips, reducing how readily they can be compared to an idealised flaw. Estimations of interaction measures for faults may have to take into account the significant shear strength of faults resulting from brecciated rock inside the fault. The traction-free surface of the Earth also provides an additional stress perturbation if the scale of the fractures is comparable to their depth [*Roering et al.*, 1997].

SIF perturbations also occur as a result of heterogeneity in the medium [*Yu et al.*, 2009]. Heterogeneity is a key aspect of geological materials which can be easily incorporated in mechanical models by variation of material properties such as the Young's modulus or Poisson's ratio. This effect could be quantified using interaction measures as more general tools to study the way SIFs are perturbed. Care must be taken in order to differentiate between perturbations induced by heterogeneity, and perturbations induced by fracture interaction, because K_i^{int} will include both of these effects. This can be accomplished

by calculating K_i^{int} in a volume containing all the fractures and material property variations, then calculating two versions of K_i^{iso} per fracture - one with the material property variations and one without. Then, separate values of C, M_i and ϵ_i can be found, each one describing the SIF perturbation arising from either heterogeneity and interaction. Such an analysis would facilitate understanding of the competing effects of interaction and heterogeneity on growth.

6.2 Computational considerations

The number of simulations needed to acquire a full dataset with n fixed fractures in a volume is $n + 1$, because the system must be simulated with all fractures present, providing values for K_{I-III}^{int}, then once for each fracture, where that fracture is the only one in the volume, providing values for K_{I-III}^{iso}. Only one mesh is required for the domain, as the same mesh can be used for all calculations. The mesh does not need to be particularly refined, as the interaction measures have been shown to remain accurate for coarse meshes (Figure 8). Fracture interaction maps are relatively expensive to generate as each location of the interacting fracture requires a new mesh around the moving fracture. The method is also not restricted to using the disk-shaped domain integral method for calculating SIFs - any 3D SIF computation method, such as displacement correlation [*Branco et al.*, 2015] or displacement discontinuity [*Thomas and Pollard*, 1993], would also be effective. Variation maps can be generated using any numerical method that generates SIFs, and can be also adapted to other fields.

3D growth simulations are an additional method with potential for exploring interaction. SIF variation maps are more convenient for several reasons. SIF perturbations are reasonably computationally cheap to calculate compared to full fracture growth simulations, that may require re-meshing at every step to track the propagation of the fracture. Growth simulations rely on many non-physical parameters arising as a result of the particular modelling technique, such as the extension increment per step, which has a large effect on the final geometry of the fracture. Additionally, the geometry from each possible initial separation is difficult to summarize in a 2D plot, unlike interaction measures which provide one numerical value per location.

6.3 Recommended use of interaction measures

The interaction measures and maps detailed in this work can be used to better understand the behavior of fractures. For an outcrop or subsurface system where fracture geometries are known, examining the SIFs and interaction measures on each fracture provides a straightforward method for summarizing their behavior. Interaction maps are more useful when the locations of fractures are either variable or unknown, such as when fractures are blind, or across large outcrops. Maps shown in this work demonstrate their effectiveness at highlighting geometries which result in enhanced, reduced or non-planar growth. They can also be created for any pair of fractures with different geometries and orientations. Therefore, rather than referring to a catalog of maps, they should be created to fit the relative fracture orientations which are frequently encountered in a specific geological setting, following the steps outlined in Section 5.

It should be noted that C and M do not directly determine the increased likelihood of propagation without additional context, such as material toughness. This can instead be approached by using a critical stress intensity factor for the material, which, if reached by K_I, results in fracture propagation [*Atkinson*, 1984]. This value can be used to scale the results of the output, or in the place of K_i^{iso} to show when fractures are close enough to cause propagation. However, those results will be dependent on the properties of the medium, unlike the maps presented here, which are material and scale-invariant.

6.4 Contrasting C and M_i

C and M_i both characterise the magnitude of interaction experienced by a fracture. C yields consistent quantifications of interaction across different levels of mesh refinement. Because it is derived from comparing the area beneath two curves, its magnitude is independent of the magnitude of stress. This makes C the most convenient measure for assessing whether interaction occurs using a threshold. The benefits of using M_i are that the calculation is simple, *i.e.* it does not require numerical integration and could be found graphically, and it also provides a location on the fracture at which the SIF perturbation is highest. Either method provides similar results for how interaction changes around a fracture. In particular, the interaction map for C_I in Figure 10 is almost identical to M_I in Figure 11.

A benefit of using C will be when a system contains multiple close fractures. This would create a complex distribution of SIFs around the tip with multiple peaks and troughs, which would be fully captured by C, but only one peak would be selected for M_i. Looking at the modes individually is also important because, in overlapped geometries, there may be multiple peaks and troughs in all three modes. Therefore, in most cases C is the recommended measure.

7 Conclusions

This work provides several contributions towards analysing and understanding fracture interaction processes through study of the stress intensity factor (SIF) perturbations. These perturbations occur when two or more fractures are close enough to alter the state of stress at one another's tips. Using a 3D finite element based fracture mechanics model simulating pairs of fractures, these perturbations have been demonstrated and quantified. Three measures of interaction have been proposed to quantify how the SIFs are altered - 'circumferential SIF perturbation' (C), 'maximum SIF perturbation' (M_i) 'amplification to shielding ratio' (ϵ). C and M_i can be used to quantify the magnitude of the interaction, and ϵ can be used to describe whether the stress at the tip of a fracture is mostly amplified or shielded. These measures have been used to study the interaction occurring around pairs of fractures of equal size in several orientations. This is accomplished by creating interaction maps, which plot measures of interaction in space according to the location of an interacting fracture. The analysis outlined in this work, and the interaction measures that are proposed, are applicable to any stress state or fracture population. This provides a new and powerful way to understand how fractures affect one another.

References

Anderson, T. L., and T. Anderson (2005), *Fracture mechanics: fundamentals and applications*, CRC press.

Atkinson, B. K. (1984), Subcritical crack growth in geological materials, *Journal of Geophysical Research: Solid Earth*, *89*(B6), 4077–4114, doi:10.1029/JB089iB06p04077.

Banks-Sills, L. (2010), Application of the finite element method to linear elastic fracture mechanics, *Applied Mechanics Reviews*, *63*(2), 020,803, doi:10.1115/1.3119488.

Banks-Sills, L., and D. Sherman (1986), Comparison of methods for calculating stress intensity factors with quarter-point elements, *International Journal of Fracture*, *32*(2), 127–140, doi:10.1007/BF00019788.

Benveniste, Y., G. J. Dvorak, J. Zarzour, and E. C. J. Wung (1989), On interacting cracks and complex crack configurations in linear elastic media, *International Journal of Solids and Structures*, *25*(11), 1279–1293, doi:10.1016/0020-7683(89)90092-9.

Brace, W. (1960), An extension of the Griffith theory of fracture to rocks, *Journal of Geophysical Research*, *65*(10), 3477–3480, doi:10.1029/JZ065i010p03477.

Branco, R., F. V. Antunes, and J. D. Costa (2015), A review on 3D-FE adaptive remeshing techniques for crack growth modelling, *Engineering Fracture Mechanics*, *141*, 170–195, doi:10.1016/j.engfracmech.2015.05.023.

Bremberg, D., and J. Faleskog (2015), A numerical procedure for interaction integrals developed for curved cracks of general shape in 3-D, *International Journal of Solids and Structures*, *62*, 144–157, doi:10.1016/j.ijsolstr.2015.02.022.

Busfield, J. J. C., V. Jha, H. Liang, I. C. Papadopoulos, and A. G. Thomas (2005), Prediction of fatigue crack growth using finite element analysis techniques applied to three-dimensional elastomeric components, *Plastics, Rubber and Composites*, *34*(8), 349–356, doi:10.1179/174328905X59728.

Carter, B. J., P. A. Wawrzynek, and A. R. Ingraffea (2000), Automated 3-D crack growth simulation, *International Journal for Numerical Methods in Engineering*, *47*(1-3), 229–253, doi:10.1002/(SICI)1097-0207(20000110/30)47:1/3<229::AID-NME769>3.0.CO;2-2.

Cherepanov, G. P. (1979), *Mechanics of brittle fracture*, McGraw-Hill, New York.

Cook, R. D., et al. (2007), *Concepts and applications of finite element analysis*, John Wiley & Sons.

Cotterell, B., and J. R. Rice (1980), Slightly curved or kinked cracks, *International Journal of Fracture*, *16*(2), 155–169, doi:10.1007/BF00012619.

Delaney, P. T., and D. D. Pollard (1981), Deformation of host rocks and flow of magma during growth of minette dikes and breccia-bearing intrusions near Ship Rock, New Mexico, *U.S. Geological Survey Professional Paper*, *1202*.

Duffy, O. B., R. E. Bell, C. A. L. Jackson, R. L. Gawthorpe, and P. S. Whipp (2015), Fault growth and interactions in a multiphase rift fault network: Horda Platform, Norwegian North Sea, *Journal of Structural Geology*, *80*, 99–119, doi: 10.1016/j.jsg.2015.08.015.

Fabrikant, V. I. (1987), Close interaction of coplanar circular cracks in an elastic medium, *Acta Mechanica*, *67*(1-4), 39–59, doi:10.1007/BF01182121.

Fan, Y., Z. Zhu, J. Kang, and Y. Fu (2016), The mutual effects between two unequal collinear cracks under compression, *Mathematics and Mechanics of Solids*, pp. 1–14, doi:10.1177/1081286515625436.

Fu, P., S. M. Johnson, R. R. Settgast, and C. R. Carrigan (2012), Generalized displacement correlation method for estimating stress intensity factors, *Engineering Fracture Mechanics*, *88*, 90 – 107, doi:10.1016/j.engfracmech.2012.04.010.

Gawthorpe, R. L., and M. R. Leeder (2000), Tectono-sedimentary evolution of active extensional basins, *Basin Research*, *12*(3-4), 195–218, doi:10.1046/j.1365-2117.2000.00121.x.

Geiger, S., S. Matthai, and S. Roberts (2001), *Complex Systems Platform: CSP3D3: user's guide*, Technical report, ETH Zurich Research Reports, doi:10.3929/ethz-a-004432279.

Grechka, V., and M. Kachanov (2006), Effective elasticity of fractured rocks: A snapshot of the work in progress, *Geophysics*, *71*(6), W45–W58, doi:10.1190/1.2360212.

Green, R. G., T. Greenfield, and R. S. White (2015), Triggered earthquakes suppressed by an evolving stress shadow from a propagating dyke, *Nature Geoscience*, *8*(8), 629–632,

doi:10.1038/NGEO2391.

Gross, D. (1982), Stress intensity factors of systems of cracks, *Ingenieur-Archiv.*, *51*, 301–310, doi:10.1007/BF00536656.

Irwin, G. R. (1956), Analysis of stresses and strains near the end of a crack traversing a plate, *Journal of Applied Mechanics*, *24*(79), 361–364.

Jing, L., and J. A. Hudson (2002), Numerical methods in rock mechanics, *International Journal of Rock Mechanics and Mining Sciences*, *39*(4), 409–427, doi:10.1016/S1365-1609(02)00065-5.

Kachanov, M. (1987), Elastic solids with many cracks: A simple method of analysis, *International Journal of Solids and Structures*, *23*(1), 23–43, doi:10.1016/0020-7683(87)90030-8.

Kachanov, M. (1993), Elastic solids with many cracks and related problems, *Advances in Applied Mechanics*, *30*, 259–445, doi:10.1016/S0065-2156(08)70176-5.

Kachanov, M., and J. P. Laures (1989), Three-dimensional problems of strongly interacting arbitrarily located penny-shaped cracks, *International Journal of Fracture*, *41*(4), 289–313, doi:10.1007/BF00018861.

Kamaya, M. (2008a), Growth evaluation of multiple interacting surface cracks. Part II: Growth evaluation of parallel cracks, *Engineering Fracture Mechanics*, *75*(6), 1350–1366, doi:10.1016/j.engfracmech.2007.07.014.

Kamaya, M. (2008b), Growth evaluation of multiple interacting surface cracks. Part I: Experiments and simulation of coalesced crack, *Engineering Fracture Mechanics*, *75*(6), 1336–1349, doi:10.1016/j.engfracmech.2007.07.015.

Kassir, M. K., and G. C. Sih (1975), *Mechanics of Fracture 2, Three-Dimensional Crack Problems*, Noordhoff International Publishing, Leyden.

Lam, K., and S. Phua (1991), Multiple crack interaction and its effect on stress intensity factor, *40*(3), 585–592, doi:10.1016/0013-7944(91)90152-Q.

Laures, J.-P., and M. Kachanov (1991), Three-dimensional interactions of a crack front with arrays of penny-shaped microcracks, *International Journal of Fracture*, *48*(4), 255–279, doi:10.1007/BF00012916.

Lawn, B. R. (1993), *Fracture of Brittle Solids*, Cambridge University Press.

Legrand, L., and V. Lazarus (2015), Front shape and loading evolution during cracks coalescence using an incremental perturbation method, *Engineering Fracture Mechanics*, *133*, 40–51, doi:10.1016/j.engfracmech.2014.10.026.

Lei, Q., J.-P. Latham, and C.-F. Tsang (2017), The use of discrete fracture networks for modelling coupled geomechanical and hydrological behaviour of fractured rocks, *Computers and Geotechnics*, *85*, 151–176, doi:10.1016/j.compgeo.2016.12.024.

Lisjak, A., and G. Grasselli (2014), A review of discrete modeling techniques for fracturing processes in discontinuous rock masses, *Journal of Rock Mechanics and Geotechnical Engineering*, *6*(4), 301–314, doi:10.1016/j.jrmge.2013.12.007.

Liu, F., and R. I. Borja (2008), A contact algorithm for frictional crack propagation with the extended finite element method, *International Journal for Numerical Methods in Engineering*, *76*(10), 1489–1512, doi:10.1002/nme.2376.

Moussa, W. A. (2002), Investigating the Interaction Behavior Between Two Arbitrarily Oriented Surface Cracks Using Multilevel Substructuring, *Journal of Pressure Vessel Technology*, *124*(4), 440, doi:10.1115/1.1465439.

Nakamura, T., and D. Parks (1988), Three-dimensional stress field near the crack front of a thin elastic plate, *ASME, Transactions, Journal of Applied Mechanics*, *55*, 805–813, doi:10.1115/1.3173725.

Nejati, M., A. Paluszny, and R. W. Zimmerman (2015a), A disk-shaped domain integral method for the computation of stress intensity factors using tetrahedral meshes, *International Journal of Solids and Structures*, doi:10.1016/j.ijsolstr.2015.05.026.

Nejati, M., A. Paluszny, and R. W. Zimmerman (2015b), On the use of quarter-point tetrahedral finite elements in linear elastic fracture mechanics, *Engineering Fracture Mechanics*, *144*, 194–221, doi:10.1016/j.engfracmech.2015.06.055.

Nejati, M., A. Paluszny, and R. W. Zimmerman (2016), A finite element framework for modeling internal frictional contact in three-dimensional fractured media using unstructured tetrahedral meshes, *Computer Methods in Applied Mechanics and Engineering*, *306*, 123–150, doi:10.1016/j.cma.2016.03.028.

Nelson, R. (2001), *Geologic analysis of naturally fractured reservoirs*, Gulf Professional Publishing.

Olson, J. E. (2004), Predicting fracture swarms - the influence of subcritical crack growth and the crack-tip process zone on joint spacing in rock, *Geological Society, London, Special Publications*, *231*(1), 73–88, doi:10.1144/GSL.SP.2004.231.01.05.

Olson, J. E., and D. D. Pollard (1991), The initiation and growth of en echelon veins, *Journal of Structural Geology*, *13*(5), 595–608, doi:10.1016/0191-8141(91)90046-L.

Paluszny, A., and S. K. Matthäi (2009), Numerical modeling of discrete multi-crack growth applied to pattern formation in geological brittle media, *International Journal of Solids and Structures*, *46*(18), 3383–3397, doi:10.1016/j.ijsolstr.2009.05.007.

Paluszny, A., and R. W. Zimmerman (2011), Numerical simulation of multiple 3D fracture propagation using arbitrary meshes, *Computer Methods in Applied Mechanics and Engineering*, *200*(9), 953–966, doi:10.1016/j.cma.2010.11.013.

Paluszny, A., and R. W. Zimmerman (2013), Numerical fracture growth modeling using smooth surface geometric deformation, *Engineering Fracture Mechanics*, *108*, 19–36, doi:10.1016/j.engfracmech.2013.04.012.

Paris, P. C., and F. Erdogan (1963), A Critical Analysis of Crack Propagation Laws, *Journal of Basic Engineering*, *85*(4), 528, doi:10.1115/1.3656900.

Philip, Z. G., J. W. Jennings, J. E. Olson, S. E. Laubach, J. Holder, et al. (2005), Modeling coupled fracture-matrix fluid flow in geomechanically simulated fracture networks, in *SPE Annual Technical Conference and Exhibition, 29 September-2 October, San Antonio, Texas*, vol. 8, pp. 300–309, Society of Petroleum Engineers, doi:10.2118/77340-MS.

Pouya, A. (2015), A finite element method for modeling coupled flow and deformation in porous fractured media, *International Journal for Numerical and Analytical Methods in Geomechanics*, *39*(16), 1836–1852, doi:10.1002/nag.2384.

Price, N., and J. Cosgrove (1990), *Analysis of Geological Structures*, Cambridge University Press.

Rabczuk, T. (2013), Computational Methods for Fracture in Brittle and Quasi-Brittle Solids: State-of-the-Art Review and Future Perspectives, *International Scholarly Research Notices: Applied Mathematics*, *2013*(849231), 1–38, doi:10.1155/2013/849231.

Renshaw, C. E., and D. D. Pollard (1994), Numerical simulation of fracture set formation: A fracture mechanics model consistent with experimental observations, *Journal of Geophysical Research*, *99*(B5), 9359–9372, doi:10.1029/94JB00139.

Riahi, A., E. R. Hammah, and J. H. Curran (2010), Limits of applicability of the finite element explicit joint model in the analysis of jointed rock problems, in *44th US Rock Mechanics Symposium - 5th US/Canada Rock Mechanics Symposium*, American Rock Mechanics Association.

Rice, J. R. (1968), A path independent integral and the approximate analysis of strain concentration by notches and cracks, *Journal of Applied Mechanics*, *35*(2), 379–386, doi:10.1115/1.3601206.

Rives, T., M. Razack, J.-P. Petit, and K. Rawnsley (1992), Joint spacing: analogue and numerical simulations, *Journal of Structural Geology*, *14*(8-9), 925–937, doi:10.1016/0191-8141(92)90024-Q.

Roering, J. J., M. L. Cooke, and D. D. Pollard (1997), Why blind thrust faults do not propagate to the Earth's surface: Numerical modeling of coseismic deformation associated with thrust-related anticlines, *Journal of Geophysical Research: Solid Earth*, *102*(B6), 11,901–11,912, doi:10.1029/97JB00680.

Rooke, D. P., and D. J. Cartwright (1976), *Compendium of stress intensity factors*, Procurement Executive, Ministry of Defence. H. M. S. O.

Salimzadeh, S., A. Paluszny, and R. W. Zimmerman (2017), Three-dimensional poroelastic effects during hydraulic fracturing in permeable rocks, *International Journal of Solids and Structures*, *108*, 153–163, doi:10.1016/j.ijsolstr.2016.12.008.

Shih, C. F., H. G. de Lorenzi, and M. D. German (1976), Crack extension modeling with singular quadratic isoparametric elements, *International Journal of Fracture*, *12*(4), 647–651, doi:10.1007/BF00034654.

Stonesifer, R., F. Brust, and B. Leis (1993), Mixed-mode stress intensity factors for interacting semi-elliptical surface cracks in a plate, *Engineering Fracture Mechanics*, *45*(3), 357–380, doi:10.1016/0013-7944(93)90021-J.

Stüben, K. (2001), A review of algebraic multigrid, *Journal of Computational and Applied Mathematics*, *128*(1), 281–309, doi:10.1016/S0377-0427(00)00516-1.

Thomas, A. L., and D. D. Pollard (1993), The geometry of echelon fractures in rock: implications from laboratory and numerical experiments, *Journal of Structural Geology*, *15*(3-5), 323–334, doi:10.1016/0191-8141(93)90129-X.

Thomas, R. N., A. Paluszny, and R. W. Zimmerman (2017), Fracture interaction data supporting Thomas et al. 2017, 'Quantification of fracture interaction using stress intensity factor variation maps', National Geoscience Data Centre, British Geological Survey, doi: 10.5285/1c36b573-4c63-4d5b-8372-534843d2454a.

Tsang, C.-F., I. Neretnieks, and Y. Tsang (2015), Hydrologic issues associated with nuclear waste repositories, *Water Resources Research*, *51*(9), 6923–6972, doi: 10.1002/2015WR017641.

Walters, M. C., G. H. Paulino, and R. H. Dodds (2005), Interaction integral procedures for 3-d curved cracks including surface tractions, *Engineering Fracture Mechanics*, *72*(11), 1635–1663, doi:10.1016/j.engfracmech.2005.01.002.

Wiesner, C., S. Maddox, W. Xu, G. Webster, F. Burdekin, R. Andrews, and J. Harrison (2000), Engineering critical analyses to BS7910 - the UK guide on methods for assessing the acceptability of flaws in metallic structures, *International Journal of Pressure Vessels and Piping*, *77*(14), 883–893, doi:10.1016/S0308-0161(01)00011-4.

Yan, X. (2010), A boundary element analysis for stress intensity factors of multiple circular arc cracks in a plane elasticity plate, *Applied Mathematical Modelling*, *34*(10), 2722–2737, doi:10.1016/j.apm.2009.12.008.

Yau, J. F., S. S. Wang, and H. T. Corten (1980), A Mixed-Mode Crack Analysis of Isotropic Solids Using Conservation Laws of Elasticity, *Journal of Applied Mechanics*, *47*(2), 335, doi:10.1115/1.3153665.

Yu, H., L. Wu, L. Guo, S. Du, and Q. He (2009), Investigation of mixed-mode stress intensity factors for nonhomogeneous materials using an interaction integral method, *International Journal of Solids and Structures*, *46*(20), 3710–3724, doi: 10.1016/j.ijsolstr.2009.06.019.

Zachariasen, J., and K. Sieh (1995), The transfer of slip between two en echelon strike-slip faults: A case study from the 1992 Landers earthquake, southern California, *Journal of Geophysical Research*, *100*(B8), 15,281, doi:10.1029/95JB00918.

Zhan, S., and T. Wang (2006), Interactions of penny-shaped cracks in three-dimensional solids, *Acta Mechanica Sinica/Lixue Xuebao*, *22*(4), 341–353, doi:10.1007/s10409-006-0007-8.